Exploring the formation of intrinsic *p*-type and *n*-type defects in CuO

Aleksandar Živković [1,2] and Nora H. de Leeuw [2,3,*]

[1] *Cardiff University, School of Chemistry, Main Building Park Place, Cardiff CF10 3AT, United Kingdom*

[2] *Department of Earth Sciences, Utrecht University, Princetonlaan 8a, 3548CB Utrecht, The Netherlands*

[3] *School of Chemistry, University of Leeds, Woodhouse Lane, Leeds LS2 9JT, United Kingdom*

(Received 5 December 2019; revised 5 June 2020; accepted 8 July 2020; published 28 July 2020)

CuO (cupric oxide) is a well-known *p*-type semiconductor, suitable for solar cell photovoltaic applications. However, due to the easy formation of defects and Cu-rich layers at the copper(II) oxide heterointerface, commercial application is yet to be successfully implemented. Density functional theory calculations have been employed to study the formation of intrinsic defects and their effect on the electronic properties of CuO. Native impurities were observed, depending on the synthesis conditions, to render the conductivity to *p*-type or *n*-type at a low energetic cost, yet with states embedded deep in the electronic band gap. Respective defect pairs, effectively determining the majority charge carriers, were observed to cluster in near proximity of each other, lowering the formation energy substantially. Hydrogen passivation was illustrated to have a positive effect on deep defect states in *p*-type CuO, without affecting the *n*-type counterpart. Outlined results were found to support the experimentally observed low photoresponse of CuO and further illustrate some of the difficulties related with achieving high-performance samples.

DOI: 10.1103/PhysRevMaterials.4.074606

I. INTRODUCTION

Copper(II) oxide (CuO) is a strongly correlated transition-metal oxide which shows active coupling between spin, charge, orbital, and vibrational degrees of freedom. It has been studied intensively since the discovery of cuprate high-temperature superconductors due to the close resemblance of its structural, electronic, and magnetic properties [1–4]. In CuO, low-energy physics induces antiferromagnetism with two distinct Néel temperatures and multiferroicity, reflecting the presence of competing equilibrium phases lying close to each other in energy [5–7].

CuO is a *p*-type semiconductor with promising potential as a nontoxic, stable, and abundant material for photovoltaic (PV) and photocatalytic applications. Owing to its favorable electronic band-gap value of 1.4 eV [8–10], it was postulated as an ideal candidate for solar harvesting technologies. However, reports on CuO solar cells are relatively rare, and the obtained power conversion efficiencies (PCE) of incident sunlight into usable electric currents yield values which are an order of magnitude lower than the estimated potential value based on the Shockley-Queisser limit (around 30 %) [11]. As demonstrated earlier [12–14], one single ideal value does not guarantee good applicability for solar harvesting (especially for oxides of copper), as this neglects a multitude of other factors (recombination, strong absorption onset, charge-carrier lifetimes, etc.).

In practice, many photovoltaic energy converters use semiconducting materials in the form of a *p*-*n* or *p*-*i*-*n* junction. Structures of heterojunction solar cells with *p*-type CuO typically involve *n*-type Si, although their efficiencies measure values below 0.5% [15]. The low performance was attributed to the formation of Cu-rich copper oxide, as well as an amorphous interfacial oxide layer occurring between CuO and Si. Slight improvement was observed in Al/Ti/*n*-Si/*p*-CuO/Ti/Al heterostructure solar cells, approaching efficiencies of 1% [16]. Doping CuO with N and interfacing with *n*-Si was observed to improve the efficiency to 1.21% as a result of improved crystallinity and thinning of the interfacial Cu-rich layer [17].

It was not until recent that *n*-type CuO has been observed. This conductivity type, driven by an excess number of electrons, was detected in nanoscale nonstoichiometric CuO_x deposited by reactive magnetron sputtering [18]. By depositing *n*-CuO_x onto hydrogenated amorphous Si, efficiencies of 3.04% and 4.78% were observed. Efficiency values were enhanced because in this case the interfacial Cu-rich layer acts as an electron supply reservoir instead of a recombination source for holes in *p*-CuO.

Du *et al.* [19] have reported single-phase intrinsic *n*-type CuO films prepared by magnetron sputtering combined with a high-voltage and low-current technique. Increasing the substrate temperature was found to convert CuO from a *p*-type semiconductor at 75 °C (348 K) to an *n*-type semiconductor at 500 °C (773 K). The *n*-type conductivity was assigned to oxygen vacancies and interstitial copper atoms. Enhanced point-defect scattering rates with increasing temperature were identified as the main cause of the decrease in overall carrier mobility rates with increasing temperature. Singh *et al.* [20] have reported the successful deposition of *n*-type CuO via spin coating. *n*-type CuO was created at moderate oxygen partial pressures (metal excess phase), leaving the material oxygen-deficient in the form of oxygen vacancies. The annealing time was reported to be a crucial parameter, with CuO changing into Cu_2O over a prolonged time. Further studies of *n*-type

*Corresponding author: N.H.deLeeuw@leeds.ac.uk

CuO included extrinsic impurity-driven conductivity change. Baturay and co-workers [21] observed *p*-type conductivity conversion into *n*-type in CuO thin films when doped with Co. Capacity-voltage measurements verified a change in polarity at 3% doping ratio, with no change in the band gap. Moreover, Wang *et al.* [22] observed increased charge separation and transfer in a CuO semiconducting photocathode as a result of a simple O_2 treatment which rendered the material's conductivity *p* type.

Theoretically, despite a substantial number of publications studying the ground-state properties of CuO, the intrinsic defects still remain largely unexplored. Nolan and Elliott [23] and Wu *et al.* [24] studied the native defects within CuO using LSDA + U calculations. However, defects were studied in the conventional monoclinic cell and simple antiferromagnetic configuration, not necessarily corresponding to the experimentally observed ground state. More recently, Wang *et al.* [22] explored the influence of copper vacancies in CuO-based photocathodes using the general gradient approximation–Perdew-Burke-Ernzerhof, GGA(PBE) + U calculations. Nonetheless, none of the reported studies concerning the formation of defects in CuO took into account the formation of competing phases, namely, Cu_2O and Cu_4O_3, thereby most likely representing growth conditions for unphysical CuO compositions.

In the current work, native point defects, both simple and complex, were initialized within the magnetic unit cell of CuO and their formation energies, and the influence on the overall electronic band structure was explored. In order to do so, a comparative density functional theory (DFT) study was undertaken using Hubbard-corrected and hybrid exchange correlation functional approximations. An attempt to answer some of the following questions is made here: (i) Which defects occur intrinsically in CuO and which computational method describes them accurately? (ii) Does the model address the origin of experimentally observed *n*-type conductivity, and if so, under which conditions?

II. COMPUTATIONAL DETAILS

The results computed and presented in this work were were obtained from spin-polarized DFT-based calculations performed with the Vienna *Ab-initio* Simulation Package (VASP) [25]. The interactions between core and valence electrons were represented using the projector augmented wave (PAW) method [26]. The GGA [27] exchange-correlation (XC) functional with PBE parametrization was employed for DFT + U within the formalism of Dudarev *et al.* [28]. For the hybrid-DFT calculations, the Heyd-Scuseria-Ernzerhof (HSE) XC functional was used [29–31], with a screening parameter of 0.2 $Å^{-1}$. Long-distance dispersion corrections were included using the D3 approach of Grimme *et al.* [32]. The plane-wave expansion cutoff was set to 450 eV, and the force convergence criterion to cell relaxation was 0.01 eV/Å. Γ-centred Monkhorst-Pack [33] meshes ($3 \times 5 \times 3$ for a magnetic unit cell and a single Γ point for the $2 \times 3 \times 2$ supercell) were employed to sample the Brillouin zone in reciprocal space. Band structure calculations were performed on the optimized structure along high-symmetry directions obtained from the Bilbao Crystallographic Server [34–36] and plotted using the WANNIER90 code [37,38]. The phase stability diagram of CuO for a range of accessible chemical potentials was computed using CPLAP (Chemical Potential Limits Analysis Program) [39], taking into account its limiting competing phases. The extent of defect charge distribution was studied using the Bader scheme as implemented in the Henkelman code [40–42]. Suitable defect positions were identified using the PYCDT package [43], and graphical drawings were produced using VESTA [44].

The values for the effective Hubbard parameter (U_{eff}) and the amount of the nonlocal exact Hartree-Fock exchange used within the HSE XC functional were tuned according to the value of the ground-state electronic band gap and (spin only) magnetic moment of the respective Cu atoms. Excitonic and spin-orbit coupling effects were not taken into account.

The formation energy of a defect X in charge state q is defined as [45,46]

$$E^f[X^q] = E_{\text{tot}}[X^q] - E_{\text{tot}}[\text{bulk}] - \sum_i n_i\mu_i + q\left(E_F + \varepsilon^{\text{H}}_{\text{VBM}}\right) + E_{\text{corr}}. \quad (1)$$

$E_{\text{tot}}[X]$ is the total energy derived from a supercell calculation containing the defect X, and $E_{\text{tot}}[\text{bulk}]$ is the total energy for the perfect crystal using an equivalent supercell. The integer n_i indicates the number of atoms of type i (host atoms or impurity atoms) that have been added to ($n_i > 0$) or removed from ($n_i < 0$) the supercell to form the defect, and μ_i are the corresponding chemical potentials of the considered species (related through $\Delta\mu_i = \mu_i - \mu_i^\circ$, where μ_i° is the chemical potential of the element i in its standard phase). The chemical potentials represent the energy of the reservoirs with which atoms are being exchanged. E_F represents the electron chemical potential, which ranges from the valence to the conduction band edges, and $\varepsilon^{\text{H}}_{\text{VBM}}$ is the eigenvalue of the valence-band maximum of the pristine bulk material. Finally, E_{corr} is a correction term that accounts for the finite-size effect in the calculations of charged defects as well as aligning of the band edges between the bulk and the defective supercells, performed using the SXDEFECTALIGN code by Freysoldt *et al.* [47]. The thermodynamic transition levels (ionization levels) of a given defect, $\varepsilon(q_1/q_2)$, correspond to the Fermi-level position at which a given defect changes from one charge state (q_1) to another (q_2):

$$\varepsilon(q_1/q_2) = \frac{E^f[X^{q_1}] - E^f[X^{q_2}]}{q_2 - q_1}. \quad (2)$$

The allowed values of $\Delta\mu_i$ are determined from a set of thermodynamic limits. The upper limit is given by $\Delta\mu_i \leqslant 0$, where element i precipitates to its standard state, e.g., O_2(g) (referred to half of the total energy of an oxygen molecule) and Cu(s). Also, to avoid the formation of secondary solids, the chemical potentials must also be bound by

$$2\Delta\mu_{\text{Cu}} + \Delta\mu_{\text{O}} \leqslant \Delta H_{\text{f}}(\text{Cu}_2\text{O}), \quad (3)$$

$$4\Delta\mu_{\text{Cu}} + 3\Delta\mu_{\text{O}} \leqslant \Delta H_{\text{f}}(\text{Cu}_4\text{O}_3), \quad (4)$$

with ΔH_{f} being the standard enthalpy of formation at zero K. The total energies of the phases competing with CuO, i.e., Cu_2O and Cu_4O_3, were calculated using their respective

unit cells. Cu_2O was modeled in a simple cubic nonmagnetic cell, while for tetragonal Cu_4O_3, a primitive cell containing 14 atoms was used together with the antiferromagnetic spin ordering leading to the observed lowest energy configuration [48–50]. The calculated formation energies of CuO, Cu_2O, and Cu_4O_3 read –1.58 eV (1.35 eV), –1.70 eV (–1.46 eV), and –4.85 eV (–4.15 eV), calculated using DFT + U (HSE), and are considerably close to experimental values of 1.59 eV [51], –1.75 eV [51], and –4.88 eV [52], respectively.

In the case of CuO passivation, the solubility of the H species was limited by the formation of an additional compound, copper(II) hydroxide:

$$\Delta\mu_{\mathrm{Cu}} + 2\Delta\mu_{\mathrm{O}} + 2\Delta\mu_{\mathrm{H}} = \Delta H_{\mathrm{f}}[\mathrm{Cu(OH)_2}]. \quad (5)$$

III. RESULTS AND DISCUSSION

A. Modelling magnetic CuO

CuO crystallizes in a lower symmetry monoclinic crystal structure (space group $C2/c$, number 15) compared to Cu_2O. The conventional unit cell consists of eight atoms, four Cu atoms and four O atoms. Each copper atom is coordinated by four oxygen atoms in an approximately square planar configuration, while each oxygen atom is located at the center of a distorted tetrahedron [53], with the following lattice parameters: a = 4.6837 Å, b = 3.4226 Å, c = 5.1288 Å [54]. Below 230 K, the magnetic ground state of CuO is a peculiar antiferromagnetic arrangement. This ordering is described within an eight-formula magnetic unit cell (Fig. 1) whose lattice vectors are obtained by expanding the conventional unit-cell lattice vectors via the relation $\mathbf{a}' = \mathbf{a} + \mathbf{c}$, $\mathbf{b}' = \mathbf{b}$, and $\mathbf{c}' = -\mathbf{a} + \mathbf{c}$ [6].

As previously demonstrated by Rödl *et al.* [6], the local magnetic moments that occur both on the Cu and O atoms, as well as the electronic band gap, can be tuned depending on the screened exchange parameter (α) in hybrid (HSE) or as a function of the on-site interaction U in PBE + U calculations. Moreover, a majority of works available in the literature employ experimental lattice parameters within their simulations, which ensures consistency between calculated and experimental crystal structures. However, experimental geometries are (usually) not identical to minimum-energy geometries obtained by structural relaxations within a given functional. This issue is particularly pronounced when hybrid density functionals are employed [55], where calculation time increases dramatically (in the range of a thousandfold) and system size is limited to a few dozen atoms.

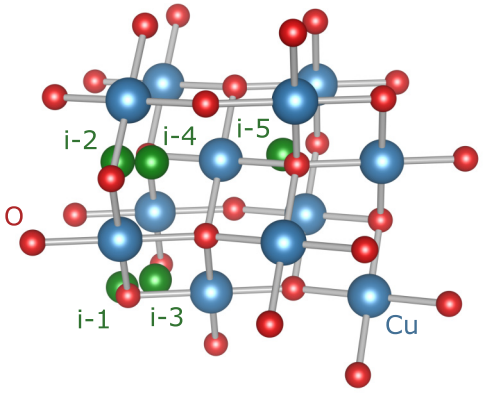

FIG. 1. Crystal structure of the magnetic unit cell of CuO together with the five identified suitable positions for interstitial atoms.

In order to examine the underlying effects of strain remnants within the magnetic CuO simulation cell, various prerelaxed, atomically relaxed, and fully relaxed geometries were tested and their validity assessed. Furthermore, two differently ordered spin arrangements of the Cu^{2+} ions in CuO were considered, one along the z axis (AF_Z, the most stable magnetic state) and one along the x axis (AF_X). These were taken following the nomenclature outlined by Rocquefelte *et al.* [1] to allow for easier comparison and validation with earlier works.

First, the influence of the U_{eff} parameter within DFT + U and the exact exchange α within hybrid DFT on the electronic (Kohn-Sham) band gap were assessed. Results for the two distinct magnetic arrangements are summarized in Fig. 2. Note the different values of U_{eff} and α when fitting to the electronic band gap. For a fit to the low-temperature band-gap value of 1.3–1.5 eV [56], a value of $U_{\mathrm{eff}} = 5$ eV and $U_{\mathrm{eff}} = 7$ eV can be read for the AF_Z and AF_X magnetic ordering, respectively. Similarly, for hybrid DFT calculations, values of $\alpha \approx 0.125$ and $\alpha \approx 0.175$ used within HSE are read for AF_Z and AF_X. This explains the variety of U_{eff} and α values in the existing literature that were used for bulk CuO calculations. Together with the choice of an appropriate simulation cell and magnetic arrangement, defining a unique simulation setup becomes a question of the physical properties under examination.

Furthermore, so far the simulations have included relaxation effects only up to the atomic position level, i.e., lattice parameters and the cell volume were kept fixed. Starting from the experimental lattice parameters of the CuO magnetic unit cell with two different magnetic arrangements, calculations allowing for lattice cell shape relaxation were performed in order to circumvent the observed internal pressure left within the geometry of the system after only atomic relaxation was performed. The pressure was in certain cases as high as ±2 GPa (20 kbar), depending on the system under study. Such values are large enough to drive lattice instabilities and subsequent structural phase transitions [57]. Thus, care must be taken in order to avoid and minimize internal lattice stress when dealing with CuO. Results of those simulations are illustrated in Fig. 3. Based on those results and discussion outlined above, values of $U_{\mathrm{eff}} = 5.5$ eV for DFT + U and $\alpha = 0.125$ for HSE were chosen for this study, as they reproduce the electronic band gap and magnetic moments values accurately, minimizing the internal pressure simultaneously. Surprisingly, by allowing for the lattice parameters to change during the relaxation run of AF_X, the calculations proceed in such way that it converges to the AF_Z geometry, indirectly confirming the most stable magnetic configuration.

B. Intrinsic defects of CuO

To explore the native defects in CuO, an antiferromagnetic $2 \times 3 \times 2$ supercell (starting from the magnetic unit cell) was created, which ensures minimal interaction

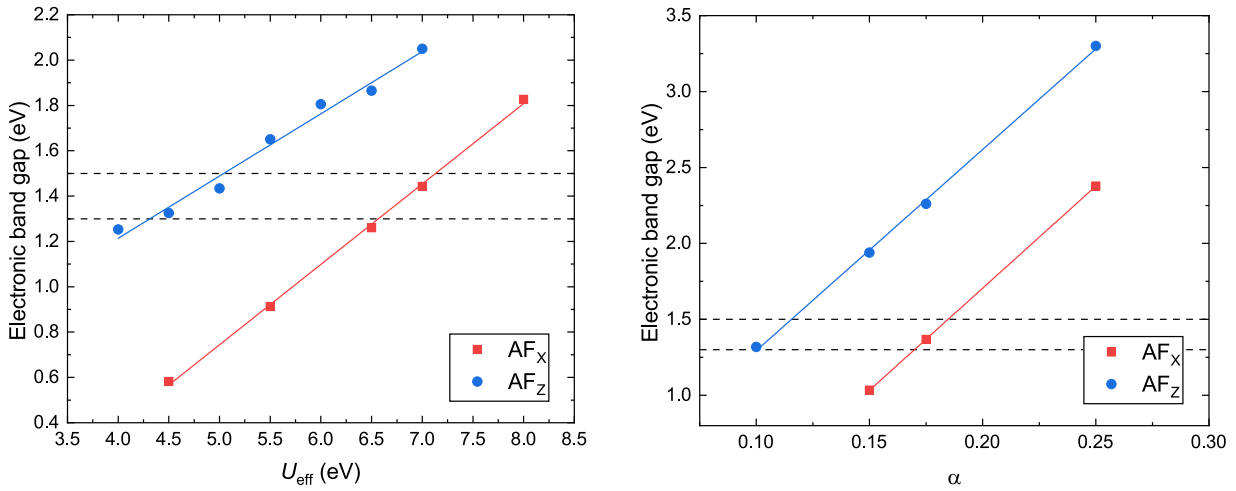

FIG. 2. The electronic band-gap dependence on the effective U parameter within DFT + U (left) and the exact exchange amount α used for hybrid DFT calculations (right). The red-filled squares refer to the AF_X magnetic arrangement, while the blue-filled dots represent the AF_Z magnetic configuration. The linear fit is merely an eye-guide for easier data readout. The dashed black lines indicate the range of experimentally available low-temperature values.

between introduced defects, located at least 10 Å apart in each crystallographic direction. Furthermore, the differences between DFT + U and HSE values of defect formation energies and impurity band positions within the electronic structure are examined.

a. Phase stability. Following the formalism outlined in Eqs. (1)–(4), the boundaries for chemical potentials were calculated and shown in Fig. 4. To analyze the effect of employed growth conditions on undoped CuO samples, two chemical potential limits were chosen: one with O-rich/Cu-poor and the other with Cu-rich/O-poor conditions. The selected values read

(1) O-rich/Cu-poor: $\Delta\mu(\mathrm{Cu}) = -1.594$, $\Delta\mu(\mathrm{O}) = 0.000$.

(2) Cu-rich/O-poor: $\Delta\mu(\mathrm{Cu}) = -0.157$, $\Delta\mu(\mathrm{O}) = -1.437$.

Simple native defects were introduced into the CuO magnetic supercell, including simple vacancies (labeled V_{Cu} and V_O), antisites (Cu_O and O_{Cu}), and interstitials in various positions within the cell (Cu_i and O_i).

b. Intrinsic defects. Figure 5 displays the neutral formation energies for all the possible intrinsic defects occurring in CuO. It is observed that the formation energy of defects varies depending on growth environments but features overall similar trends between DFT + U and HSE. Under Cu-rich growth environments, the most favorable neutral defects are V_O and Cu_i, with the hindmost depending on the position within the cell. On the other hand, under O-rich conditions, p-type defects V_{Cu}, O_{Cu}, and O_i (which unlike their Cu counterparts do not depend on the position within the cell) are favored over all n-type defects. The differences in formation

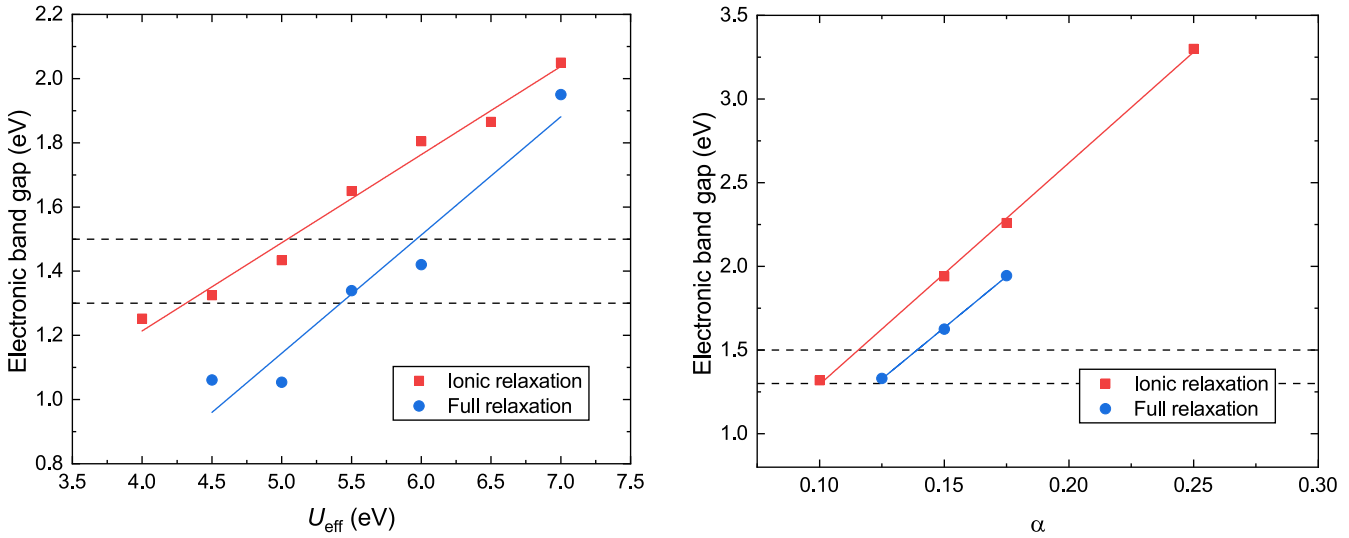

FIG. 3. The electronic band-gap dependence on the effective U parameter (left) and the exact exchange amount α (right) for the AF_Z configuration. The red-filled squares refer to the atomically relaxed geometry, while the blue-filled dots represent the fully relaxed geometry (incorporating atomic, cell, and volume relaxation). The linear fit is merely an eye-guide for easier data readout. The dashed black lines indicate the range of experimentally available low-temperature values.

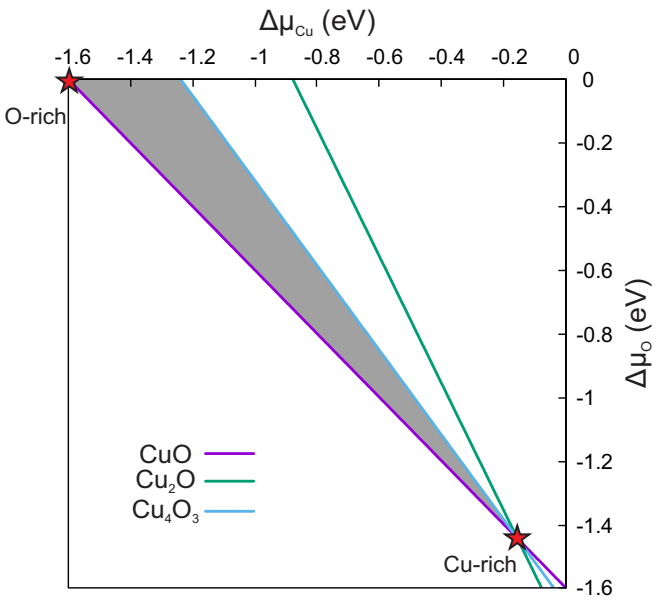

FIG. 4. CuO stability limits in the range of allowed chemical potentials, emphasized within the gray-shaded area. The points highlighted with red stars indicate the chemical potential taken for the calculations to be carried out. Values were calculated from experimental formation enthalpies in order to assure transferability of results.

energies between distinct growth conditions are large enough to allow for high-performance undoped samples of CuO with particular conductivity types to be created.

Figure 6 presents a cumulative schematic diagram drawn from electronic densities of state for the considered defects within CuO, obtained using DFT + U and HSE calculations. Similar to the formation energies, the overall trends are consistent between DFT + U and HSE calculations, with the absolute values varying slightly. It is evident that the majority of defects introduce states within the electronic band gap of CuO that are far from the band edges. Such states are detrimental to the operation of devices relying on the promotion of electrons via photon absorption, as they act as recombination centers rather then contributing to an increase in carriers. In order to explore the full potential of intrinsic defects on the carrier generation and compensation processes in CuO, the formation energies of intrinsic defects in various charged states was studied. A plot of the defect formation energy as a function of the Fermi-level position for both considered growth environments is plotted in Fig. 7. Since the difference between the two utilized methods, DFT + U and HSE, was shown to be small, further discussions concern only results based on HSE calculations.

In a Cu-rich environment, the most prominent intrinsic donors are V_O and Cu_i with formation energies around 1 eV. However, V_O behaves as a deep donor, with a $\varepsilon(+1/0)$ transition level at 0.69 eV above the valence-band maximum (VBM). Such behavior of V_O in CuO corresponds well to the extremely low carrier mobility of (0.482–1.727) cm^2 V^{-1} s^{-1} measured in n-type CuO [19]. Cu_i, despite requiring less energy than V_O, forms exclusively as a neutral defect, with its ionization level located in the VBM, and is thus unlikely

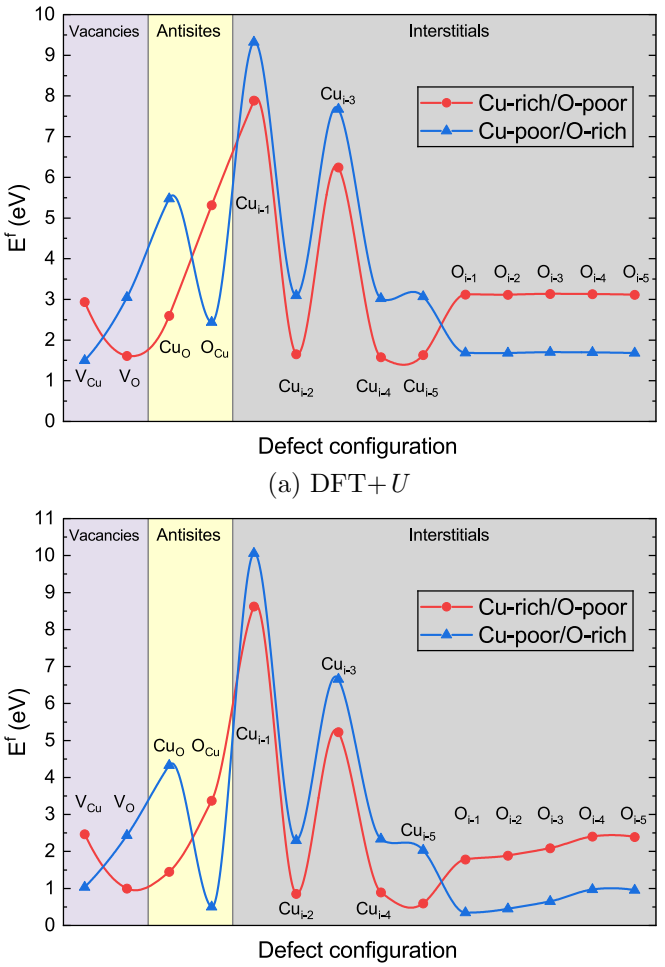

(a) DFT+U

(b) HSE

FIG. 5. Calculated formation energies of simple native defects in CuO under different chemical potential limits using two types of approximation for the XC functional. Symbols are the calculated values; the lines are aides to guide the eye.

to provide effective charge compensation in CuO. The lowest energy acceptor defect under Cu-rich conditions is V_{Cu}, yet it lies too high in energy to compensate for the most prominent donor impurities.

Under O-rich conditions, acceptor defects dominate the native impurity landscape. The lowest energy acceptor is the O_i, which together with the O_{Cu} and V_{Cu} are all found to form up to 1 eV. Over the whole range of the electronic band gap, those are not compensated by any other defects, rendering the material entirely p type in nature. V_{Cu} acts as a relatively shallow acceptor with the $\varepsilon(0/-1)$ transition at 0.17 eV above the VBM and a subsequent deeper $\varepsilon(-1/-2)$ transition at 0.28 eV below the conduction band minimum (CBM). O_{Cu} demonstrates two deep acceptor levels, $\varepsilon(0/-1)$ at 0.49 eV and $\varepsilon(-1/-2)$ at 1.07 eV above the VBM. The calculated $\varepsilon(0/-1)$ transition level of the O_i is found at 1.14 eV above the VBM, thus limiting the otherwise high conductivity that could be expected due to the very low cost involved in the formation of these defects.

These results confirm the experimentally observed n-type conductivity of CuO, assigned to O vacancies and interstitial

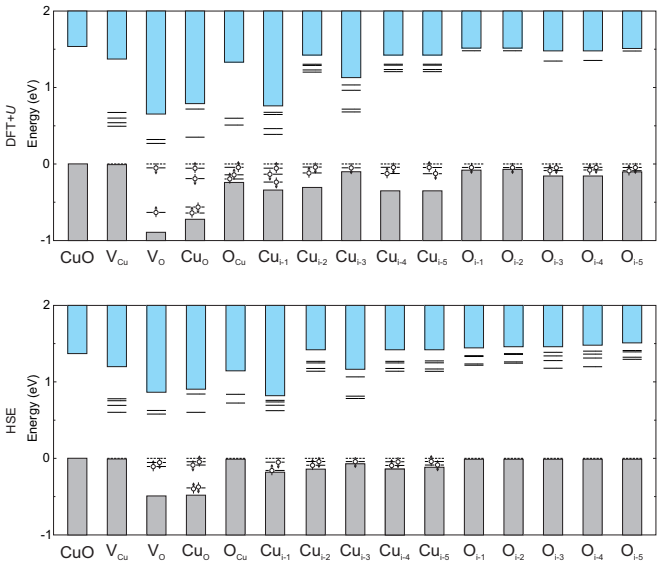

FIG. 6. A cumulative schematic representation drawn from electronic densities of state (DOS) data calculated for clean and defective CuO. A comparison between DFT + U and HSE calculated values is illustrated in the top and bottom row. The gray and light-blue rectangular shapes correspond to the valence and conduction band, respectively, while short lines indicate positions of defect levels obtained from DFT + U and HSE calculations. The dashed line indicates the highest occupied band, and up/down arrows represent different spin channels.

Cu atoms [19,20], as well as p-type conductivity assigned to Cu vacancies [21]. Unlike the case of Cu_2O, depending on the growth conditions, CuO can intrinsically be created as an n-type (Cu-rich/O-poor environment) or p-type (O-rich/Cu-poor environment) semiconductor. However, explored defects present in CuO show states deep in the electronic band gap,

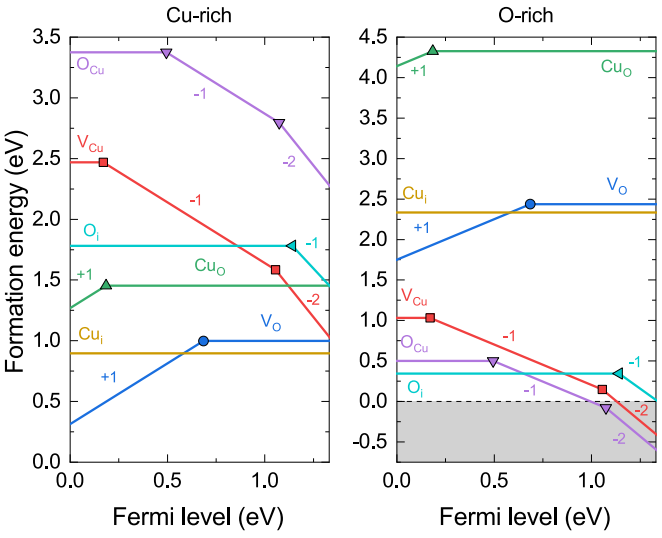

FIG. 7. Calculated defect formation energies as a function of the Fermi-level position of native defects occurring in CuO under different chemical potential limits. The slope of the lines denotes the charge state, and the solid dots represent the transition levels ε.

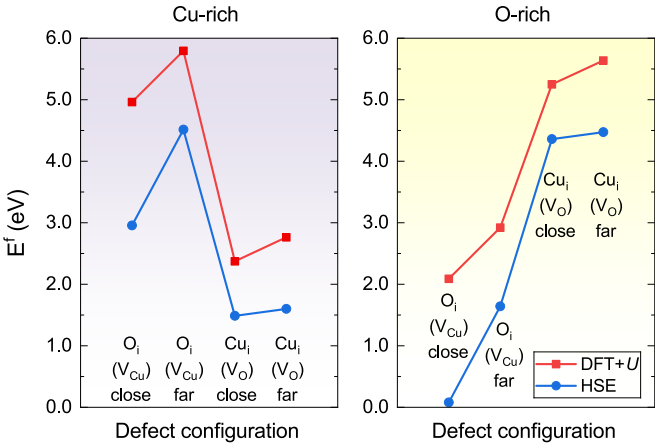

FIG. 8. Formation energies for pairs of defects within CuO under different growth conditions. The used notation specifies a newly induced defect into a cell where the one enclosed in brackets is already present. The pairs were chosen according to the lowest formation energies of individual defects illustrated earlier. A trend to form small clusters can be observed both under Cu-rich and O-rich conditions. Symbols are the calculated values; the lines are aides to guide the eye.

thus acting as recombination and trap states rather then carrier concentration and mobility promoters.

c. The formation of defect pairs. Since a clear trend in occurrence of distinct defects is observed, V_{Cu} or O_i under O-rich and V_O or Cu_i under Cu-rich conditions, there is a question of whether these defects would appear simultaneously. In order to verify this suggestion, defect pairs were introduced into the simulation cell. Pairs were chosen according to the lowest formation energy of their individual appearance under specific growth conditions. In addition, the possibility of clustering effects was analyzed by introducing defects in close proximity to each other and as far away as possible across the simulation cell.

The calculated formation energies for neutral pairs of defects in CuO is shown in Fig. 8. From these results, a clear trend of defect clustering over dispersion is noted, regardless of the nature of the defect or employed computational scheme. Furthermore, particular defect formation in close proximity demonstrates a lowering of the formation energy compared to the sum of individual energies. For example, under Cu-rich conditions, the creation of a Cu interstitial next to an already present O vacancy requires an energy of 2.38 eV (1.49 eV), which is lower compared to the sum of individual defect formation energies $E^f(\mathrm{Cu}_i) + E^f(\mathrm{V}_O) = 1.58\,(0.99)\,\mathrm{eV} + 1.61\,(0.89)\,\mathrm{eV} = 3.19\,(1.88)\,\mathrm{eV}$, calculated using DFT + U (HSE).

First, the case where defects are maximally dispersed through the cell is analyzed. The two defects were placed at a minimum distance of 8.32 Å in the case of $O_i(V_{Cu})$ and 8.44 Å for $Cu_i(V_O)$, which ensures that the overlap of respective wave functions is minimized as far as possible within the supercell. The notation implies a defect introduced in the host cell where the defect written in brackets was already present. As expected, defects introduced far away across the cell do not interact significantly with each other. They localize around

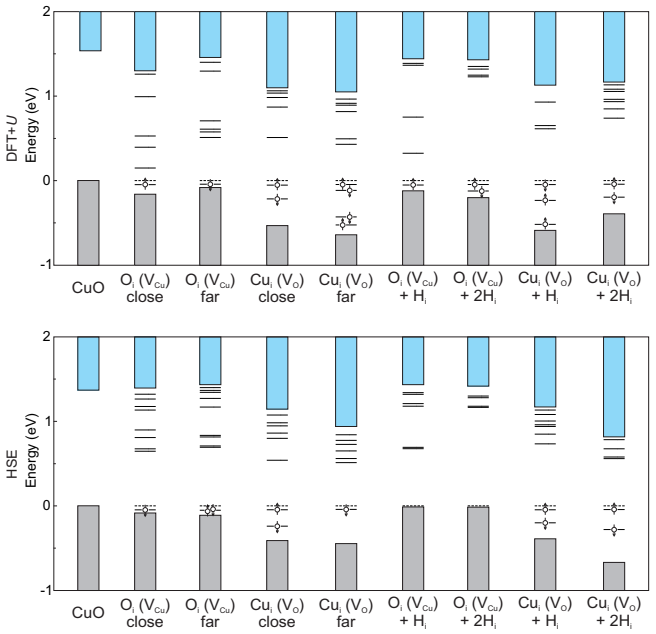

FIG. 9. A cumulative schematic representation drawn from electronic densities of state (DOS) data calculated for clean, pairwise defective, and passivated CuO. A comparison between DFT + U and HSE calculated values is illustrated in the top and bottom row. The gray and light-blue rectangular shapes correspond to the valence and conduction bands, respectively, while short lines indicate positions of defect levels obtained from DFT + U and HSE calculations. The dashed line indicates the highest occupied band, and up/down arrows represent different spin channels.

the defect site, creating individual local distortions discussed in earlier paragraphs for single impurities, as observed in the electronic densities of state in Fig. 9.

Defects occurring in close proximity to each other exhibit different properties compared to their dispersed analogs due to strong overlap of interacting impurity wave functions. For $O_i(V_{Cu})$, the newly introduced O interstitial atom distorts the structure around the defect site negligibly and forms a weak bond with the nearest lattice O atom (1.37 Å, which is comparable to the separation length of the O_2 molecule of 1.208 Å [58]). $O_i(V_{Cu})$ acts as a deep acceptor, with the $\varepsilon(0/-1)$ and $\varepsilon(-1/-2)$ transition levels found at 0.56 and 0.95 eV above the VBM, respectively.

In contrast, the addition of Cu_i around an existing V_O defect does not distort the structure significantly. The Cu_i relaxes into the void left behind by the vacancy, easing the bond stress induced by the interstitial on the nearest O and Cu atoms. This allows the structure to relax into a more ordered one, hence lowering the formation energy of the defect complex by almost 0.80 eV (0.40 eV), as indicated before, obtained for DFT + U (HSE). The migration of the interstitial Cu proceeds until a position where the Coulomb repulsion of the surrounding electrons (left behind in the created O vacancy) is minimal. The $Cu_i(V_O)$ complex behaves as a deep donor, analogous to the simple V_O, with the difference that the $\varepsilon(+1/0)$ ionization level is found nearer to the VBM, at 0.34 eV, compared to the individual O vacancy.

Following this discussion, a general tendency of defect clustering in CuO is observed. More importantly, defects tend to create states located in the middle of the band gap, which is detrimental for any application requiring effective charge capture and separation processes. Deep states favor recombination of created carriers, impairing the overall conductivity, regardless of it being n type or p type.

d. Intentional passivation. A further question emerging is whether the midgap states created by intrinsic impurities can be removed while maintaining the desired conductivity type. One mechanism through which one could influence the character of an impurity is called *passivation*. It explains the often observed compensating nature of defects when donor dopants attract impurities of the opposite kind—acceptors, and vice versa. The resulting complex is often charge neutral and electrically inactive.

In order to test the system for eventual passivation effects, hydrogen was incorporated interstitially into the CuO matrix with the most stable defects present, as identified earlier. Hydrogen was chosen as the simplest possible impurity in order to track the changes that a single electron/hole induce onto the defect complex. Furthermore, the ambiguity when modeling hydrogen is drastically reduced compared to transition-metal atoms or complex molecules, which often rely on additional U_{eff} parametrization or exact exchange tuning.

In the initial setup, one H atom is placed into the vacancy site of the $O_i(V_{Cu})$ defect complex (favoring p-type conductivity). After structural relaxation, the (effectively interstitial) H atom migrates towards the nearest-neighboring O closest to the vacancy site. The H atom binds onto one of the three dangling O bonds left after the $O_i(V_{Cu})$ defect complex was formed. This removes the strain present in the cell along the c direction, and the nearest atoms surrounding the H site relax into their original crystallographic positions in a cell without defects. However, two O dangling bonds along the a axis remain present, with reduced repulsion effects due to their missing analogs in the perpendicular direction. More importantly, two acceptor states were removed from the electronic structure when compared to the case without interstitial H (Fig. 9).

Adding a further H atom into the vacancy site of the $[O_i(V_{Cu}) + H]$ complex generates defect behavior similar to the case of a single interstitial H. The newly added H binds onto its nearest-neighboring O atom left unpaired after the Cu vacancy was created. The surrounding structure remains largely unaffected, with the two interstitial H atoms relaxing away from each other due to active repulsion between identical charges. More importantly, this defect complex configuration leads to removal of the impurity states previously present in the middle of the band gap, leaving an electronic structure similar to that of simple interstitial O atoms, as observed from Fig. 9.

Figure 10 depicts a plot of the defect formation energy as a function of the Fermi-level position for the H-passivated complexes under Cu-rich and O-rich conditions. The singly H-passivated $O_i(V_{Cu})$ defect behaves as an amphoteric defect with a shallow $\varepsilon(+1/0)$ transition level 0.03 eV above the VBM and a very deep $\varepsilon(0/-1)$ transition at 0.50 eV above the VBM, effectively killing both p-type and n-type conductivity in the system. However, the $[O_i(V_{Cu}) + 2H]$ complex is

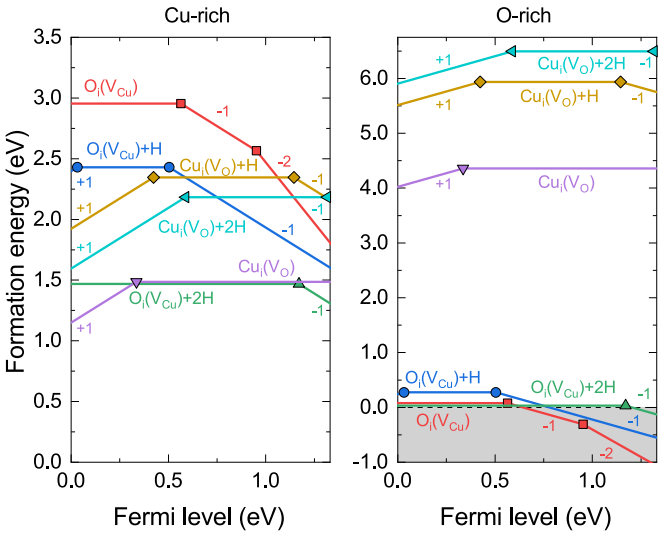

FIG. 10. Calculated formation energies as a function of the Fermi-level position of clustered and passivated defects occurring in CuO under different chemical potential limits outlined earlier. The slope of the lines denotes the charge state, and the solid dots represent the transition levels ε.

found to have only one level in the band gap, the relatively shallow $\varepsilon(0/-1)$ transition at 0.16 eV below the CBM. This unanticipated finding suggests that a varying amount of incorporated H can lead to substantially different defect behavior in CuO.

These results for CuO indicate consistent behavior with those of earlier studies on Cu_2O, where a (H–V_{Cu}) complex was found to be the most stable defect with a formation energy of only 0.17 eV (results obtained using a HSE functional with 27.5% of exact exchange) [59]. Furthermore, H_i in Cu_2O was found to be an amphoteric impurity under both sets of conditions, suppressing both *p*-type and *n*-type conductivity.

In the second considered case, interstitial H is placed into the O vacancy site of the $Cu_i(V_O)$ complex. This causes the nearest-neighboring Cu atoms to relax away from the interstitial site. The resulting electronic structure remains largely unaltered, as noted from Fig. 9.

Inserting an additional H into the vacancy site results in a stronger relaxation of surrounding atoms compared to the single H interstitial. The added H migrates into the layer beneath the O vacancy (along the $-a$ crystallographic axis), binding onto an O atom, causing the nearest-neighboring Cu to relax towards the vacant O site. More importantly, the initial electronic structure of the $Cu_i(V_O)$ complex remains unaffected. The two states remain present in the band gap, as a consequence of the inability of H to counterbalance the larger structural distortion originating from the interstitial Cu atom introduced in the first place. Both the $[Cu_i(V_O)+H]$ and $[Cu_i(V_O)+2H]$ defect complexes demonstrate amphoteric behavior, with the simultaneous presence of donor and acceptor states in the band-gap region. Also, a shifting trend of the $\varepsilon(+1/0)$ and $\varepsilon(0/-1)$ transitions towards higher Fermi levels can be noted with increasing H concentration.

Finally, the difference in passivation effects under different growth environments is discussed. Under O-rich conditions, *p*-type defects dominate the impurity landscape of H-doped CuO. With an increasing H content, *n*-type defects are becoming prohibitively expensive to create, with formation energies reaching more than 6 eV. Thus interstitial H acts as a *p*-type promoter for CuO created in an O-rich environment. In contrast, under Cu-rich conditions, the formation energy of *n*-type defects increases with H doping, while at the same time the formation energy of *p*-type defects decreases. With increasing H content, the *n*-type defects are not only compensated for but rather fully replaced by their *p*-type analogs, as observed from Fig. 10.

IV. CONCLUSION

A systematic comparative theoretical study of the DFT + U and hybrid–DFT formalism on the electronic and magnetic properties of CuO was undertaken. Various modeling parameters, such as the simulation cell, relaxation type, and magnetic configuration, were optimized before the introduction of native point defects, both simple and complex, within the magnetic unit cell of CuO, followed by the evaluation of formation energies, as well as the effect on the overall electronic structure. Following the presented analysis, several significant conclusions can be drawn:

(1) Both DFT + U and HSE are able to describe the ground state of CuO accurately. However, care is required when tuning either the U parameter in DFT + U or α in HSE according to the type of simulation that is being undertaken.

(2) Furthermore, both DFT + U and HSE approximation yield similar trends in the formation energies of simple defects that are accessible for CuO.

(3) Intrinsically, CuO can be created either *p* or *n* type, depending on the synthesis conditions employed. Despite their favorable formation energies, both *p*-type and *n*-type intrinsic defects show states embedded deep in the band gap, clarifying the ineffective photoresponse utilization noted experimentally.

(4) Interstitial H is identified as a *p*-type promoter for CuO created under O-rich conditions, at the same time being detrimental for CuO formed under Cu-rich conditions suppressing all *n*-type intrinsic defects.

One of the main drawbacks while assessing the validity of the results outlined in this chapter is the lack of experimental evidence. Unlike Cu_2O, for which various spectroscopic measurements of intrinsic defects are available, literature for CuO is scarce. Nevertheless, calculations reproduce well the observed conductivity types and the intrinsic defects underpinning them. It is expected that these results will stimulate further experimental attempts to obtain relevant transition levels and doped samples to further optimize the use of CuO as a photoresponsive material.

Information on the data underpinning the results presented here, including how to access them, can be found in the Cardiff University data catalog [60].

ACKNOWLEDGMENTS

We acknowledge the Cardiff University School of Chemistry for a Ph.D studentship for A.Z. and the Royal Society DfID Africa Program for funding. This work was

performed using the computational facilities of the Advanced Research Computing at Cardiff (ARCCA), Cardiff University. Via our membership of the UK's HPC Materials Chemistry Consortium, which is funded by EPSRC (EP/L000202, EP/R029431), this work made use of the ARCHER facility, the UK's national high-performance computing service, which is funded by the Office of Science and Technology through EPSRCs High End Computing Program.

[1] X. Rocquefelte, M.-H. Whangbo, A. Villesuzanne, S. Jobic, F. Tran, K. Schwarz, and P. Blaha, J. Phys.: Condens. Matter **22**, 045502 (2010).
[2] H.-Y. Huang, N. A. Bogdanov, L. Siurakshina, P. Fulde, J. van den Brink, and L. Hozoi, Phys. Rev. B **84**, 235125 (2011).
[3] X. Rocquefelte, K. Schwarz, and P. Blaha, Sci. Rep. **2**, 759 (2012).
[4] X. Rocquefelte, K. Schwarz, P. Blaha, S. Kumar, and J. van den Brink, Nat. Commun. **4**, 2511 (2013).
[5] A.-M. Pradipto, R. Maurice, N. Guihéry, C. de Graaf, and R. Broer, Phys. Rev. B **85**, 014409 (2012).
[6] C. Rödl, F. Sottile, and L. Reining, Phys. Rev. B **91**, 045102 (2015).
[7] C. Rödl, K. O. Ruotsalainen, F. Sottile, A.-P. Honkanen, J. M. Ablett, J.-P. Rueff, F. Sirotti, R. Verbeni, A. Al-Zein, L. Reining, and S. Huotari, Phys. Rev. B **95**, 195142 (2017).
[8] J. Ghijsen, L. H. Tjeng, J. van Elp, H. Eskes, J. Westerink, G. A. Sawatzky, and M. T. Czyzyk, Phys. Rev. B **38**, 11322 (1988).
[9] C. Ekuma, V. Anisimov, J. Moreno, and M. Jarrell, Eur. Phys. J. B **87**, 23 (2014).
[10] S. Chatterjee, S. K. Saha, and A. J. Pal, Sol. Energy Mater. Sol. Cells **147**, 17 (2016).
[11] C. Jayathilaka, V. Kapaklis, W. Siripala, and S. Jayanetti, Appl. Phys. Exp. **8**, 065503 (2015).
[12] L. Yu and A. Zunger, Phys. Rev. Lett. **108**, 068701 (2012).
[13] L. Yu, R. S. Kokenyesi, D. A. Keszler, and A. Zunger, Adv. Energy Mater. **3**, 43 (2013).
[14] A. Živković, A. Roldan, and N. H. de Leeuw, Phys. Rev. B **99**, 035154 (2019).
[15] T. Wong, S. Zhuk, S. Masudy-Panah, and G. Dalapati, Materials (Basel, Switzerland) **9**, 271 (2016).
[16] S. Masudy-Panah, K. Radhakrishnan, H. R. Tan, R. Yi, T. I. Wong, and G. K. Dalapati, Sol. Energy Mater. Sol. Cells **140**, 266 (2015).
[17] S. Masudy-Panah, K. Radhakrishnan, A. Kumar, T. I. Wong, R. Yi, and G. K. Dalapati, J. Appl. Phys. **118**, 225301 (2015).
[18] S. H. Lee, M. Shin, S. J. Yun, and J. W. Lim, Prog. Photovoltaics Res. Appl. **23**, 1642 (2015).
[19] Y. Du, X. Gao, and X. Meng, Z. Phys. B Condens. Matter **560**, 37 (2019).
[20] R. Singh, L. Yadav, Shrey, and T. Shweta, Thin Solid Films **685**, 195 (2019).
[21] Ş. Baturay, A. Tombak, D. Batibay, and Y. S. Ocak, Appl. Surf. Sci. **477**, 91 (2019).
[22] Z. Wang, L. Zhang, T. U. Schülli, Y. Bai, S. A. Monny, A. Du, and L. Wang, Angew. Chemie Int. Ed. **58**, 17604 (2019).
[23] M. Nolan and S. D. Elliott, Phys. Chem. Chem. Phys. **8**, 5350 (2006).
[24] D. Wu, Q. Zhang, and M. Tao, Phys. Rev. B **73**, 235206 (2006).
[25] G. Kresse and D. Joubert, Phys. Rev. B **59**, 1758 (1999).
[26] P. E. Blöchl, Phys. Rev. B **50**, 17953 (1994).
[27] J. P. Perdew, K. Burke, and M. Ernzerhof, Phys. Rev. Lett. **77**, 3865 (1996).
[28] S. L. Dudarev, G. A. Botton, S. Y. Savrasov, C. J. Humphreys, and A. P. Sutton, Phys. Rev. B **57**, 1505 (1998).
[29] J. Heyd, G. E. Scuseria, and M. Ernzerhof, J. Chem. Phys. **118**, 8207 (2003).
[30] J. Heyd and G. E. Scuseria, J. Chem. Phys. **121**, 1187 (2004).
[31] J. Heyd, G. E. Scuseria, and M. Ernzerhof, J. Chem. Phys. **124**, 219906 (2006).
[32] S. Grimme, J. Antony, S. Ehrlich, and H. Krieg, J. Chem. Phys. **132**, 154104 (2010).
[33] H. J. Monkhorst and J. D. Pack, Phys. Rev. B **13**, 5188 (1976).
[34] M. I. Aroyo, J. M. Perez-Mato, C. Capillas, E. Kroumova, S. Ivantchev, G. Madariaga, A. Kirov, and H. Wondratschek, Z. Kristallogr. – Cryst. Mater. **221**, 1 (2006).
[35] M. I. Aroyo, A. Kirov, C. Capillas, J. M. Perez-Mato, and H. Wondratschek, Acta Crystallogr. Sect. A Found. Crystallogr. **62**, 115 (2006).
[36] M. I. Aroyo, J. M. Perez-Mato, D. Orobengoa, E. Tasci, G. De La Flor, and A. Kirov, Bulg. Chem. Commun. **43**, 183 (2011).
[37] G. Pizzi, D. Volja, B. Kozinsky, M. Fornari, and N. Marzari, Comput. Phys. Commun. **185**, 422 (2014).
[38] G. Pizzi, V. Vitale, R. Arita, S. Bluegel, F. Freimuth, G. Géranton, M. Gibertini, D. Gresch, C. Johnson, T. Koretsune, J. Ibanez, H. Lee, J.-M. Lihm, D. Marchand, A. Marrazzo, Y. Mokrousov, J. I. Mustafa, Y. Nohara, Y. Nomura, L. Paulatto *et al.*, J. Phys.: Condens. Matter **32**, 165902 (2019).
[39] J. Buckeridge, D. Scanlon, A. Walsh, and C. Catlow, Comput. Phys. Commun. **185**, 330 (2014).
[40] M. Yu and D. R. Trinkle, J. Chem. Phys. **134**, 064111 (2011).
[41] W. Tang, E. Sanville, and G. Henkelman, J. Phys.: Condens. Matter **21**, 084204 (2009).
[42] E. Sanville, S. D. Kenny, R. Smith, and G. Henkelman, J. Comput. Chem. **28**, 899 (2007).
[43] D. Broberg, B. Medasani, N. E. Zimmermann, G. Yu, A. Canning, M. Haranczyk, M. Asta, and G. Hautier, Comput. Phys. Commun. **226**, 165 (2018).
[44] K. Momma and F. Izumi, J. Appl. Crystallogr. **44**, 1272 (2011).
[45] C. G. Van De Walle and J. Neugebauer, J. Appl. Phys. **95**, 3851 (2004).
[46] S. B. Zhang and J. E. Northrup, Phys. Rev. Lett. **67**, 2339 (1991).
[47] C. Freysoldt, J. Neugebauer, and C. G. Van de Walle, Phys. Rev. Lett. **102**, 016402 (2009).
[48] L. Pinsard-Gaudart, J. Rodríguez-Carvajal, A. Gukasov, and P. Monod, Phys. Rev. B **69**, 104408 (2004).
[49] D. Djurek, M. Prester, D. Drobac, M. Ivanda, and D. Vojta, J. Magn. Magn. Mater. **373**, 183 (2015).
[50] J. Pierson, E. Duverger, and O. Banakh, J. Solid State Chem. **180**, 968 (2007).
[51] D. R. Lide, *CRC Handbook of Chemistry and Physics*, Internet Version 2005 (CRC Press, Boca Raton, FL, 2005).

[52] K. J. Blobaum, D. Van Heerden, A. J. Wagner, D. H. Fairbrother, and T. P. Weihs, J. Mater. Res. **18**, 1535 (2003).
[53] J. B. Forsyth and S. Hull, J. Phys.: Condens. Matter **3**, 5257 (1991).
[54] W. Y. Ching, Y. N. Xu, and K. W. Wong, Phys. Rev. B **40**, 7684 (1989).
[55] J. D. Gouveia and J. Coutinho, Electron. Struct. **1**, 015008 (2019).
[56] F. Marabelli, G. B. Parravicini, and F. Salghetti-Drioli, Phys. Rev. B **52**, 1433 (1995).
[57] C.-M. Hao, Y. Li, Q. Zhu, X.-Y. Chen, Z.-X. Wang, and Y.-L. Li, CrystEngComm **20**, 5949 (2018).
[58] H. Dietrich, Angew. Chemie **73**, 511 (1961).
[59] D. O. Scanlon and G. W. Watson, Phys. Rev. Lett. **106**, 186403 (2011).
[60] http://doi.org/10.17035/d.2019.0089582693.